ISSN 1027-4510, Journal of Surface Investigation: X-ray, Synchrotron and Neutron Techniques, 2022, Vol. 16, No. 6, pp. 943–950. © Pleiades Publishing, Ltd., 2022.
Russian Text © The Author(s), 2022, published in Poverkhnost', 2022, No. 11, pp. 20–28.

Residual Stresses in $Ce_xGd_{1-x}O_{2-y}$ Films Produced by Magnetron Sputtering

A. A. Solovyev[a, *], S. V. Rabotkin[a], A. V. Shipilova[a], D. A. Agarkov[b], I. N. Burmistrov[b], and A. N. Shmakov[c]

[a] *The Institute of High Current Electronics, Siberian Branch, Russian Academy of Sciences, Tomsk, 634055 Russia*
[b] *Osipyan Institute of Solid State Physics, Siberian Branch, Russian Academy of Sciences, Chernogolovka, Moscow oblast, 142432 Russia*
[c] *Budker Institute of Nuclear Physics, Siberian Branch, Russian Academy of Sciences, Novosibirsk, 630090 Russia*
**e-mail: andrewsol@mail.ru*

Received March 10, 2022; revised May 15, 2022; accepted May 15, 2022

Abstract—The paper focuses on the synthesis of gadolinium-doped ceria ($Ce_xGd_{1-x}O_{2-y}$) thin films on the anodes of solid oxide fuel cells by reactive dual magnetron sputtering. $Ce_xGd_{1-x}O_{2-y}$ thin films 4 μm thick are deposited in the transition and oxide modes, differing by the oxygen concentration in the vacuum chamber. Residual stresses after the film deposition and thermal annealing in air are determined by the curvature of the anode plates. Dependences are obtained between the deposition modes, residual stresses and parameters of fuel cells with the $Ce_xGd_{1-x}O_{2-y}$ electrolyte. The surface morphology and cross-section of the films are studied on a scanning electron microscope. The X-ray diffraction analysis is additionally conducted to study the structure of gadolinium-doped ceria thin films using the synchrotron radiation during 1300°C annealing. It is shown that under certain conditions of the film deposition and annealing, compressive stresses can transfer to tensile stresses, which reduces the anode plate deformation after the $Ce_xGd_{1-x}O_{2-y}$ electrolyte deposition.

Keywords: thin films, gadolinium-doped ceria, solid electrolyte, solid oxide fuel cell, magnetron sputtering, residual stresses, X-ray diffraction analysis, synchrotron radiation, high temperature annealing, stoichiometry

DOI: 10.1134/S1027451022060246

INTRODUCTION

Presently, gadolinium-doped ceria ($Ce_xGd_{1-x}O_{2-y}$) is being intensively investigated for its application as a solid oxide fuel cell (SOFC) electrolyte. The main advantage of gadolinium-doped ceria (GDC) is the ionic conductivity 4 or 5 times higher than that of yttria-stabilized zirconia (YSZ) in the temperature range of 600–800°C [1]. The ionic conductivity in GDC is provided by the oxygen vacancy diffusion after the substitution of Ce^{4+} into Gd^{3+}. Therefore, the SOFC electrolyte conductivity depends on the Gd^{3+} concentration. For example, at 500°C, the maximum conductivity is observed in the $Ce_{0.9}Gd_{0.1}O_{1.95}$ electrolyte [2]. However, a mixed ionic-electronic conductivity in the reducing medium is a disadvantage of the SOFC electrolyte. The electronic conductivity predominates at high operating temperatures ranging from 800 to 1000°C [3]. For this reason, $Ce_xGd_{1-x}O_{2-y}$ is usually used as an electrolyte at temperatures up to 650°C to synthesize low-temperature SOFCs [4]. At higher temperatures, $Ce_xGd_{1-x}O_{2-y}$ is often used as a barrier layer between the YSZ electrolyte and SOFC cathode to prevent the atom diffusion between phases [5].

Along with the electrolyte conductivity affecting the SOFC power density, its mechanical strength is of great importance during the operation. This relates in particular to anode-supported fuel cells, the electrolyte thickness of which is less than 10 μm [6]. To prevent the electrolyte from fracture during the fuel cell manufacture and operation, it is advisable to avoid critical mechanical stresses exceeding the fracture stress of ceramics.

Planar anode-supported SOFCs are usually fabricated by co-sintering thin film electrolytes and relatively thick (0.5–1 mm) anode in the temperature range of 1400–1500°C [7]. At room temperature, residual stresses in fuel cells fabricated by co-sintering of the anode/electrolyte layers, are usually caused by their difference in the thermal-expansion coefficient [8, 9]. Typical values of residual stresses in anode-supported SOFCs, range between 500 and 650 MPa at room temperature [7, 10, 11]. The mechanism of formation of residual stresses in fuel cells fabricated by co-sintering of the anode/electrolyte layers is studied rather thoroughly. There is however little information in the literature about the residual stress level in thin

film electrolytes, which occur on the anode substrates after the physical vapor deposition such as magnetron sputtering, laser ablation, and others.

Residual stresses in thin films deposited by magnetron sputtering, can be internal and thermal. The former are induced by energy particles (ions, neutral atoms) and the latter—by the thermal expansion difference of the film and substrate, if the films are deposited at a high temperature. The sputtering is based on deposition of particles having a high kinetic energy. Therefore, thin-film defects (interstitial atoms, vacancies, dislocations, etc.) appearing during the deposition process, make a significant contribution to the development of internal stresses [12]. One of the main mechanisms of the stress development in thin films deposited with the use of high-energy particles, is the atomic/ion peening mechanism [13]. During a collision with the thin film, some of adsorbed atoms can implant in the surface layer and interstitial lattice sites. This leads to the lattice distortion, excess film densification, and compressive stresses. According to [14], high temperature annealing is an effective method to reduce residual stresses. Thermal treatment of the YSZ and $Ce_xGd_{1-x}O_{2-y}$ layers after magnetron sputtering enhances their ion conductivity due to the crystallinity and density improvement [15, 16].

In this work, we investigate residual stresses in the 4-μm thick $Ce_xGd_{1-x}O_{2-y}$ electrolyte layers after its reactive magnetron sputter deposition and thermal annealing in air. Reactive magnetron sputtering is a metal target sputtering in the reactive gas medium, for example, a mixture of argon and oxygen [17]. The sputtering process can occur in three modes, namely metallic, transition, and oxide, depending on the oxygen concentration in a vacuum chamber [18]. The metallic mode implies the metal atom sputtering by argon ions at the highest deposition rate. In the transition mode, the target surface is partially covered with the oxide layer, whose thickness is uncontrollable. In this mode, the film electrolyte sputtering occurs with the oxygen deficiency. In the oxide mode, the target surface is almost completely coated with the oxide layer, that results in a drastic decrease in the film deposition rate. The film is deposited with the oxide content approaching to the stoichiometry. Usually, the transition and oxide modes are used in practice. Each mode has its own strengths and weaknesses, depending on the purpose of and requirements for the film properties. In this work, we compare residual stresses in $Ce_xGd_{1-x}O_{2-y}$ films obtained in the transition and oxide modes at different deposition rates and oxygen concentrations.

EXPERIMENTAL

The NiO/YSZ anode substrates 100 × 20 mm in size were prepared by laser cutting from 100 × 100 mm commercial anodes 700 μm thick (Kceracell Co., South Korea). The selection of the NiO/YSZ anode substrates was conditioned by their commercial availability. Dual magnetron sputtering of 99.9% purity $Ce_{0.9}Gd_{0.1}$ targets (Girmet Ltd., Russia) 100 × 300 mm in size was used for the $Ce_xGd_{1-x}O_{2-y}$ film deposition performed on the upgraded installation NNV-6.6 [19]. Sputtering of 4-μm thick films was performed in a mixture of argon and oxygen in the oxide and transition modes. The distance between the targets and substrates was ~90 mm. The vacuum chamber was evacuated with a diffusion pump down to a residual pressure of 0.01 Pa. The substrates were then heated to 450°C, which was maintained during the $Ce_xGd_{1-x}O_{2-y}$ film deposition. For the better film adhesion, the substrates were treated by Ar ions generated by the ion source with the anode layer. During the film deposition process, the pressure in the chamber was 0.2 Pa. In the transition mode, the stable film deposition was provided by the pulsed power supply APEL-M-12DU-symmetric (Prikladnaya elektronika, Russia) operating at 50 kHz frequency and 3 kW constant power. The power supply had a feedback system with the oxygen flow-control unit, which allowed the user to keep constant the discharge voltage. The argon gas rate was also constant (40 mL/min).

After the film deposition, some of the substrates were subjected to 1200°C annealing in air for 2 hours in a Nabertherm oven (Germany). The ramp-up rate was controlled at 3°C/min and then the substrates were free-cooled in the oven.

The residual stress σ_f in the thin films is determined by the substrate bending from Stoney's formula [20]:

$$\sigma_f = \frac{E_s t_s^2}{6(1-\nu_s) R_s t_f},$$

where E_s is the elastic modulus of the substrate, viz. 210 GPa [21]; t_s is the substrate thickness; ν_s is the Poisson number of the substrate, viz. 0.3 [22]; R_s is the bend radius of substrate; t_f is the film thickness.

The bend radius in Stoney's formula can be calculated from

$$R_s = \frac{R_1 R_2}{R_1 - R_2},$$

where R_1 is the bend radius of the uncoated substrate, R_2 is the is the bend radius of the coated or annealed substrate. The bend radius of the anode substrate is calculated from $R = (l^2 + 4h^2)/8h$, where l is the substrate length, h is the height. Schematic of the residual stress measurement is illustrated in Fig. 1.

High-resolution scanning electron microscopy (SEM) was carried out with a Quanta 200 3D dual beam system (FEI Company, USA) and Supra 50VP (Zeiss, Germany) to investigate the microstructure of the deposited thin films and the cation ratio in them by

using an energy dispersive X-ray analyzer at least at five points of each substrate.

The XRD analysis of the $Ce_xGd_{1-x}O_{2-y}$ thin film was conducted for the synchrotron radiation (SR) beam of the VEPP-3 storage ring, in the Siberian Synchrotron and Terahertz Radiation Centre of the Budker Institute of Nuclear Physics SB RAS, Novosibirsk, Russia. During this analysis, the substrate was heated from 30 to 1300°C at a 15°C/min velocity and then cooled at a 50°C/min velocity. During the operation, the SR wavelength was 0.172 nm. The 2θ diffraction angle of the X-ray radiation was recalculated to the angle at 0.1541 nm wavelength (CuK_α radiation) for comparing the obtained results with the diffraction data from the PDF-4+ database.

The properties of SOFCs with the magnetron sputtered $Ce_xGd_{1-x}O_{2-y}$ electrolyte, were studied on disk-shaped samples of a diameter 20 mm cut by laser from 100 × 20 mm substrates. The $La_{0.6}Sr_{0.4}CoO_3$ cathode (Kceracell Co., South Korea) with a 10 × 10 mm area was screen printed onto the electrolyte film and fired in situ during the cell test start-up. The current-voltage curves of fuel cells were obtained at 700°C, with supplying dry hydrogen to the anode and air to the cathode at constant rates of 30 and 300 mL/min, respectively. Ag mesh and Pt wires were used for the current collection from the anode and cathode.

RESULTS AND DISCUSSION

Three modes used for the $Ce_xGd_{1-x}O_{2-y}$ electrolyte film deposition differ by the oxygen concentration in the vacuum chamber and, consequently, the deposition rate (see Table 1). Figure 2 presents the dependences of the deposition rate V_d and discharge voltage U_d on the oxygen gas flow Q_{O2}. The dependence $V_d = f(Q_{O2})$ is typical for magnetron sputtering [23], i.e., a drastic decrease in the film deposition rate in the transition mode and a slight change in this rate in the oxide mode. At the metallic/transition mode interface, $V_d \approx$ 40 nm/min, but owing to the significant oxygen deficiency, the films have low transparency and black color in the visible region. At the transition/oxide mode interface, the deposition rate lowers to 7 or 8 nm/min. Transparency of the obtained films indicates to their nearly stoichiometric composition. The dependence $U_d = f(Q_{O2})$ is nonmonotonic and determined by the material properties, in particular the ion-electron emission coefficient. In the transition mode, the discharge voltage decreases from 400 to 313 V with increasing oxygen flow rate. Afterwards, it grows and reaches 500 V in the oxide mode. In this work, $Ce_xGd_{1-x}O_{2-y}$ films are synthesized at 345, 353 and 500 V discharge voltage. The film on the sample 1*O* is deposited in the oxide mode at an 8 nm/min rate. Samples 2*T* and 3*T* are obtained in the transition mode at 11 and 17 nm/min rates, respectively. And the sample 4*T* is obtained in the same conditions as the sample 2*T*.

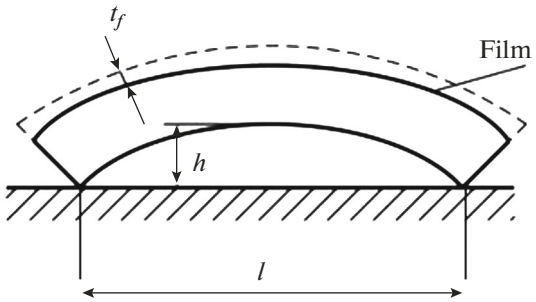

Fig. 1. Schematic of the residual stress measurement.

As can be seen from Table 1, $Ce_xGd_{1-x}O_{2-y}$ films after cooling are characterized by rather high (>2000 MPa) residual compressive stresses. The lower the oxygen flow rate during the film deposition or the higher its deficiency in the obtained film, the lower residual stresses.

We expected that after the high-temperature annealing, residual stresses reduce in $Ce_xGd_{1-x}O_{2-y}$ films. Quinn et al. [24] observed such a phenomenon in 250-nm thick YSZ films, obtained by radio-frequency sputtering, when heating up to 450°C and successive cooling to room temperature resulted in the transformation of residual compressive stresses of

Table 1. Deposition process parameters, residual stresses in $Ce_xGd_{1-x}O_{2-y}$ films, and properties of SOFCs with the magnetron sputtered $Ce_xGd_{1-x}O_{2-y}$ electrolyte

Samples	U_d, V	V_d, nm/min	t_f, μm	σ_{f0}, MPa	σ_{f1}, MPa	OCV, mV	P_{max}, mW/cm^2
1*O*	500	8	4.15	−2411	−1347	666	92
2*T*	345	11	4	−2270	−4896	636	97
3*T*	353	17	4.2	−2062	−42430	538	66
4*T*	345	11	4	−1790	2016*	693	126

*—annealing under 600 g load, O—oxide mode, T—transition mode, U_d—discharge voltage, V_d—deposition rate, t_f—film thickness, σ_{f0} and σ_{f1}—residual stresses after film deposition and 1200°C annealing, respectively; OCV—open-circuit voltage of SOFC, *P*max— maximum power density of SOFC at 700°C with electrolyte annealed at 1200°C.

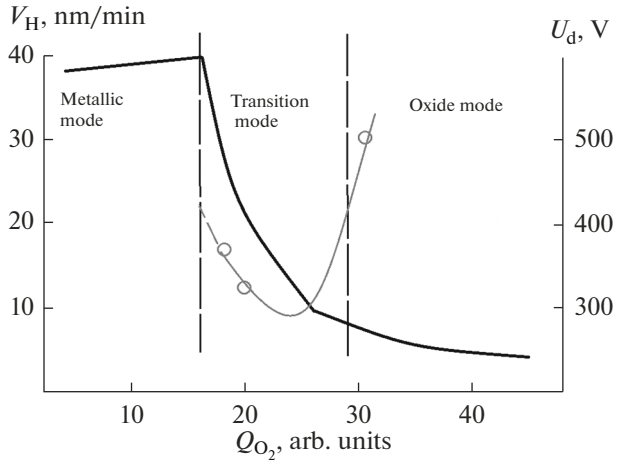

Fig. 2. Dependences of $Ce_xGd_{1-x}O_{2-y}$ film deposition rate V_H and discharge voltage U_d on the oxygen flow rate in reactive magnetron sputtering.

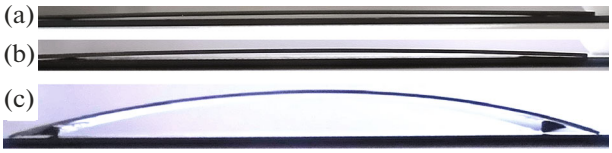

Fig. 3. Side view of NiO/YSZ samples: (a) initial sampl $3T$; (b) after $Ce_xGd_{1-x}O_{2-y}$ electrolyte film deposition, (c) after 1200°C annealing.

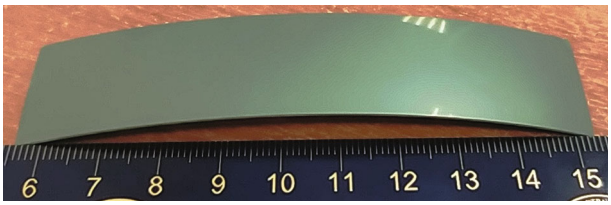

Fig. 4. Photograph of sample $3T$ coated by $Ce_xGd_{1-x}O_{2-y}$ film after 1200°C annealing.

−500 MPa into tensile stresses of 550 MPa. That could be caused by the diffusion of interstitial atoms in the standard lattice sites, which reduced the lattice distortion. Nevertheless, 1200°C annealing of $Ce_xGd_{1-x}O_{2-y}$ films led to a reduction in residual stresses down to −1347 MPa only in the sample $1O$, i.e., in the oxide mode. In samples $2T$ and $3T$, residual stresses increased up to −4896 and −42430 MPa, respectively. Thus, the oxygen deficiency in the deposited film led to the residual stress growth after its annealing and, consequently, incorporation of additional oxygen in the crystal lattice. Therefore, the higher the oxygen deficiency in the initial film, the higher residual stresses after thermal treatment.

In Fig. 3, one can see the sample $3T$ before and after the film annealing, which demonstrates the impact of residual stresses on the substrate bending. It is interesting to note that, despite very strong mechanical stresses in the film deposited onto the suample $3T$ resulting in the significant lattice distortion, the film has no visible cracks or delamination and, in Fig. 4, it manifests a perfect adhesion to the substrate.

In order to avoid an excess substrate bending, they are annealed under the dead load. Such an approach is often used in sintering laminated ceramics [25, 26]. For this, the sample $4T$ is placed between two 120 × 120 × 20 mm flat alumina plates (600 g) during annealing. Dead-load annealing provides the lower bending of the substrate $4T$ than that of the initial substrate. This indicates to the compressive-to-tensile stress transformation, the latter being 2016 MPa.

SEM observations of the surface and cross-section morphology of $Ce_xGd_{1-x}O_{2-y}$ films were conducted after 1200°C annealing to study the impact of the deposition modes. According to SEM images in Fig. 5, the surface and cross-section morphology of the annealed films was not affected by the deposition mode. The film surface consisted of 1 or 2 μm grains. Each grain comprised subgrains of a diameter ~300 nm. The cross-section surface was rich in closed pores with the size ranging between 20 and 60 nm. Due to the film recrystallization during the annealing process, pores could appear at the grain boundaries and in voids that formed during the film growth.

Figure 6 contains SEM images of the substrate $4T$ surface morphology and the cross-section microstructure after 1200°C dead-load annealing. One can see that the latter is accompanied by the compressive-to-tensile stress transformation and induces neither the film fracture nor cracking. The film structure is dense and uniform.

Since $Ce_xGd_{1-x}O_{2-y}$ films are intended for their use a the SOFC electrolyte, let us compare the current-voltage curves of the fuel cells fabricated from samples $1O$, $2T$, $3T$ and $4T$. The resulting current-voltage curves obtained at 700°C operating temperature, are collected in Table 1.

Open circuit voltage (OCV) in SOFC with the $Ce_xGd_{1-x}O_{2-y}$ electrolyte is usually below its theoretical value (1.08–1.1 V) and ranges from 0.7 to 0.8 V. This is because the electron conductivity, which appears in ceria in reducing medium. For example, OCV in SOFC with the thin-film $Ce_xGd_{1-x}O_{2-y}$ electrolyte obtained in [27] by the high-current magnetron sputtering on the similar anodes, ranges between 0.77 and 0.8 V in the operating temperature range of 600–750°C.

According to Table 1, OCV and maximum power density for $1O$, $2T$ and $3T$ samples, depend on the deposition mode of the $Ce_xGd_{1-x}O_{2-y}$ electrolyte and correlates with the residual stress values. OCV for all

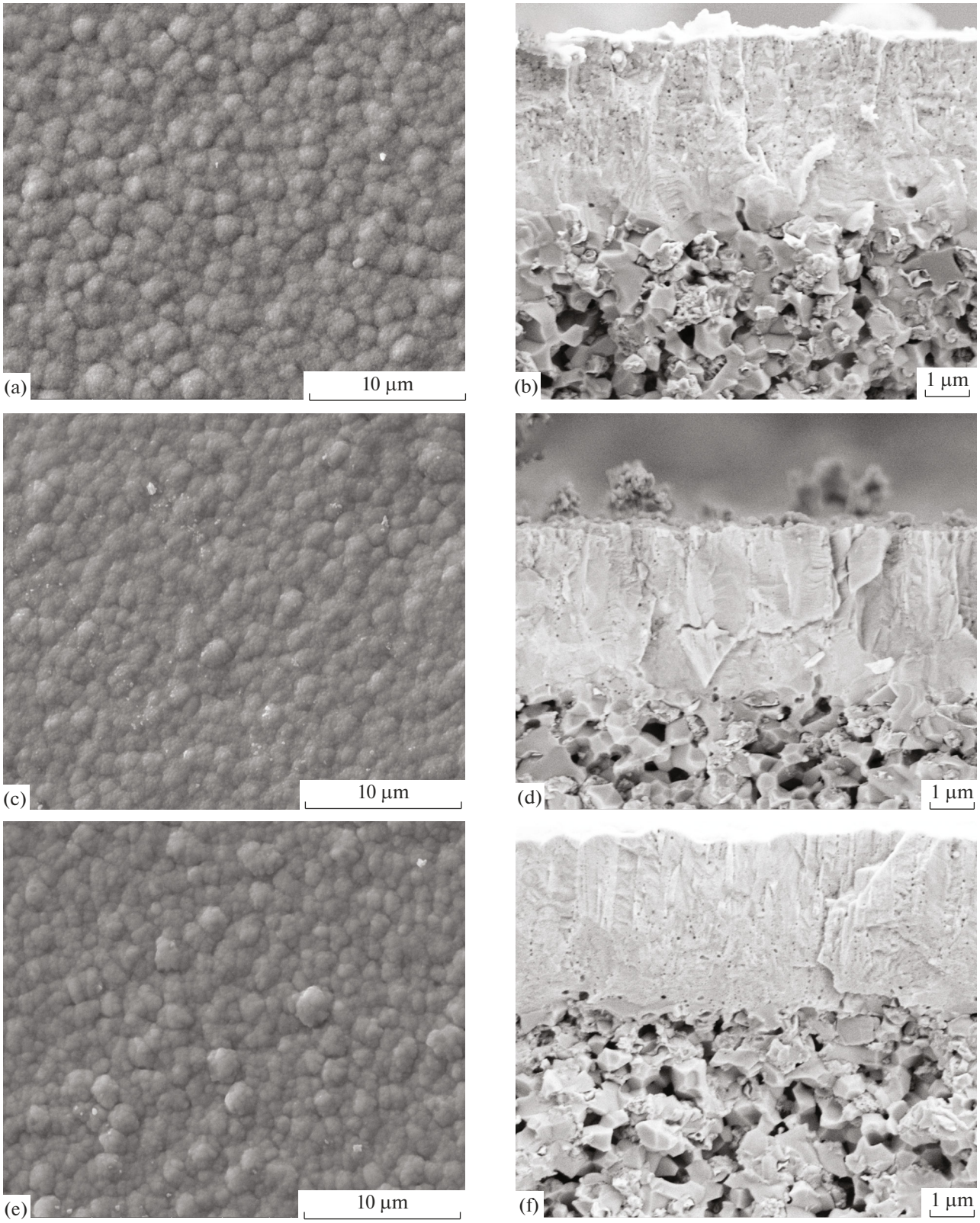

Fig. 5. SEM images $Ce_xGd_{1-x}O_{2-y}$ film surface (a, c, e) and cross-section (b, d, f) after 1200°C annealing: (a, b) sample 1*O*; (c, d) sample 2*T*; (e, f) sample 3*T*.

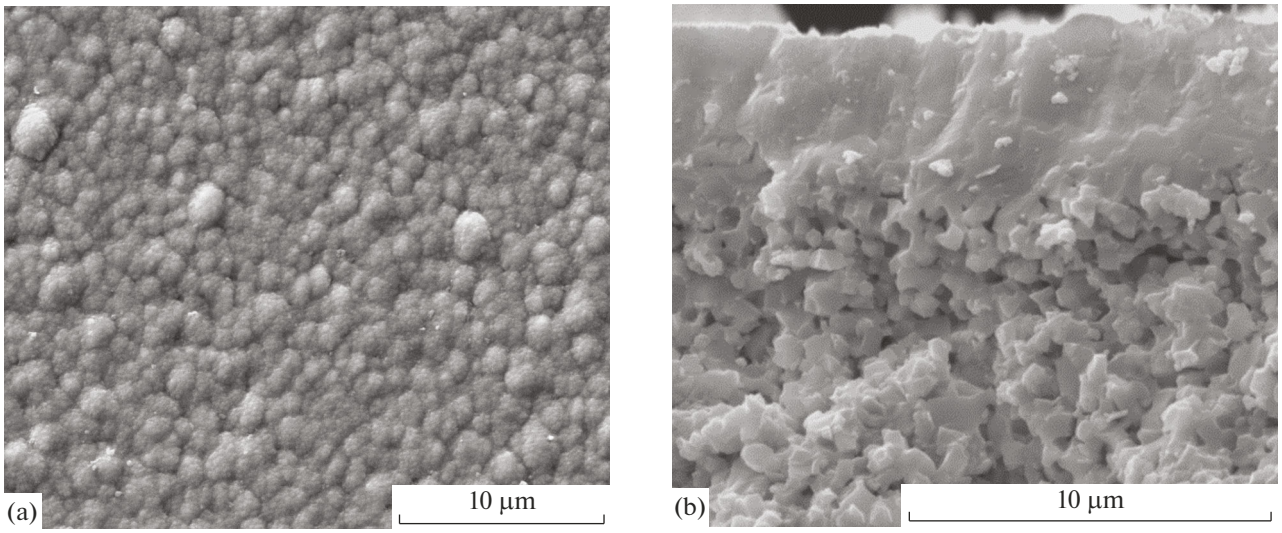

Fig. 6. SEM images of $Ce_xGd_{1-x}O_{2-y}$ film (sample 4*T*) after 1200°C dead-load annealing: (a) surface, (b) cross-section.

the substrates is below 0.7 V, which indicates to the insufficient gas impermeability for the electrolyte layer, i.e., the presence of defects not observed on SEM images or generated during heating of fuel cells up to the operating temperature. The lowest OCV (0.53 V) and the power density (66 mW/cm^2) are observed for the substrate 3*T*, which is characterized by the highest residual stresses after annealing. At the same time, the substrate 4*T* having tensile residual stresses in the electrolyte layer at room temperature, demonstrates the highest values of OCV (0.69 V) and power density (126 mW/cm^2). This means that dead-load annealing provides not only the compressive-to-tensile stress transformation, but also improved properties of the $Ce_xGd_{1-x}O_{2-y}$ electrolyte. Araki et al. [28] report that tensile stresses increase the ion conductivity of 8 mol % yttria-stabilized zirconia due to the increase in the oxygen mobility. It is assumed that mechanical stresses induce the gradient of potential energy of neighboring oxygen centers, especially around yttrium ions, which, probably, promotes the oxygen ion migration. Therefore, the impact of mechanical stresses on the electrolyte conductivity requires further investigation with a view to improve the SOFC properties.

The XRD analysis of the $Ce_xGd_{1-x}O_{2-y}$ thin film after the deposition and annealing was conducted by using the SR beam of the VEPP-3 storage ring. The high SR intensity and collimation provided high-resolution studies. The station mounted on channel No. 6 of the of the emitter terminal assisted in studying the $Ce_xGd_{1-x}O_{2-y}$ film structure obtained in the oxide mode not followed by thermal annealing.

The XRD patterns of the $Ce_xGd_{1-x}O_{2-y}$ film deposited in the oxide mode, are presented in Fig. 7. The XRD analysis shows that the unit cell parameter of the film exceeds the value given in the ICDD PDF2 database even for 0.3 doping degree. This explains the structural imperfection of the film, low values (25–28 nm) of the coherent scattering region (CSR), and high defect content. Within $2\theta = 44–60$ degrees, the (220), (311) and (222) peak intensities are detected for ceria. In Fig. 7, the diffraction peaks for the $Ce_{0.9}Gd_{0.1}O_2$ composition are given for comparison (04-002-6160 ICDD PDF database file number). The peak positions of gadolinium (10%)-doped ceria are compared because the sputtered target contains 10 at % Gd. Moreover, according to the EDX analysis (see Fig. 8), the content of 11.4 at % Gd in the film is close to that of the sputtered target. The peak shift of ceria towards the low-angle region in the initial X-ray diffraction is probably associated with residual compressive stresses observed in the film during its growth.

During 400°C annealing, the peak positions of ceria shift to the left due to the thermal expansion of the crystal lattice. Within the range of 400–700°C, these peaks shift to the right, thereby demonstrating the lattice compression. This behavior of the diffraction peaks is usually explained by the structural ordering of the material or a change in its chemical composition. At ~800°C annealing, the peak shift occurs to the left again, which indicates to further thermal expansion. After heating up to 1300°C and cooling to room temperature, the lattice parameter of the $Ce_xGd_{1-x}O_{2-y}$ film reduces down to 0.54312 nm, which is lower than its initial value. The CSR grows nearly two-fold, viz. ~49–51 nm. Ceria diffraction peaks approaching to its standard values after heating and cooling denotes the residual stress reduction in the film, which correlates with the data obtained for the substrate bending.

Wu et al. [16] also reported on the CSR growth from 18 to 26 nm after 900°C annealing of the

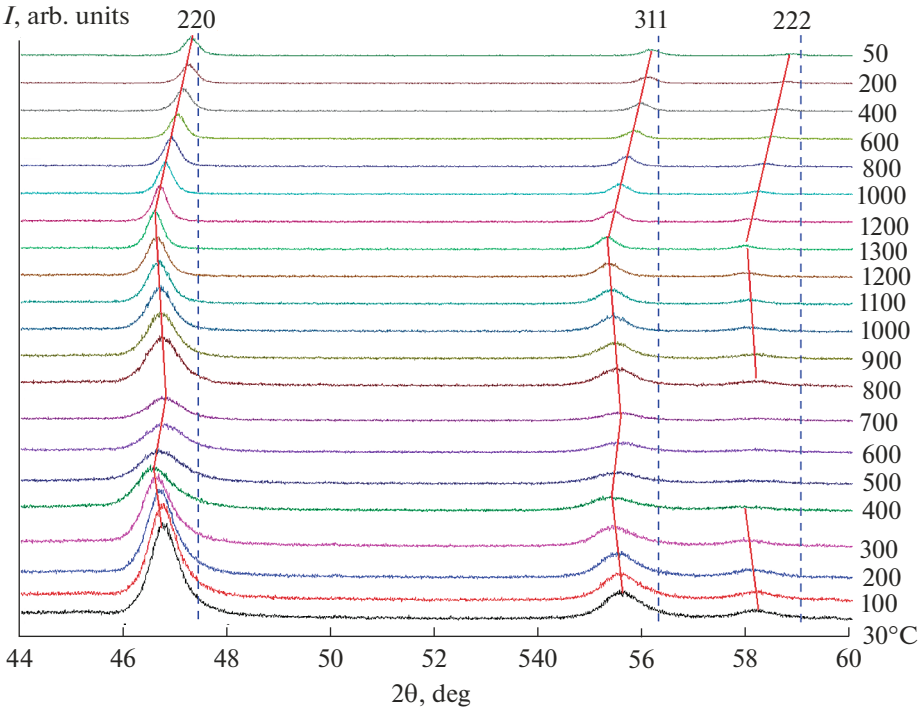

Fig. 7. In situ XRD patterns of $Ce_xGd_{1-x}O_{2-y}$ film deposited in oxide mode at heating/cooling in air. Dashed lines indicate $Ce_{0.9}Gd_{0.1}O_2$ peaks at room temperature. The ICDD PDF2 database file number for this composition is 04-002-6160.

$Ce_xGd_{1-x}O_{2-y}$ film deposited by the reactive magnetron sputtering of the target comprising 90 at % Ce and 10 at % Gd. After 900–1100°C annealing for 2 h, the ceria diffraction peaks shifted towards a large-angle region, demonstrating the decrease in the lattice parameter.

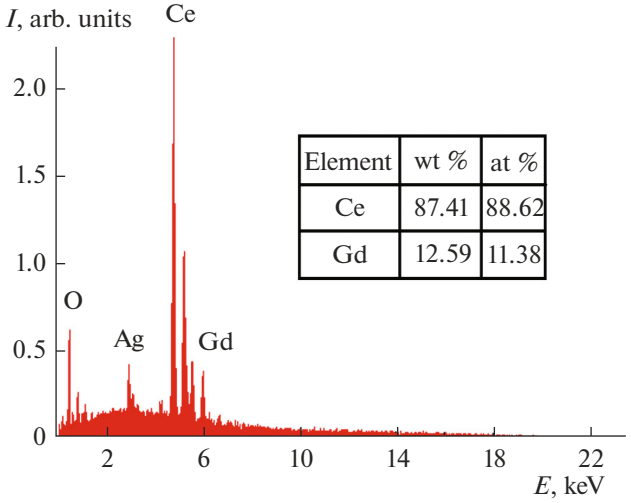

Element	wt %	at %
Ce	87.41	88.62
Gd	12.59	11.38

Fig. 8. EDX results of $Ce_xGd_{1-x}O_{2-y}$ film (1*O* substrate). Ce and Gd content is given without considering oxygen and silver atoms deposited before SEM observations.

CONCLUSIONS

The film deposition modes and high-temperature annealing in air were investigated in relation to residual stresses in the GDC films deposited by the reactive dual magnetron sputtering. Residual stresses over 2000 MPa were detected in the fabricated $Ce_xGd_{1-x}O_{2-y}$ films. The stress level depended on the oxygen deficiency in the film, such that the lowest stresses were observed in the films with the highest oxygen deficiency. 1200°C annealing in air resulted in the residual stress reduction in the films deposited in the oxide mode. The stress level increased by 2 to 20 times in the films deposited in the transition mode. It was however shown that residual stresses in the films were successfully eliminated by the dead-load annealing, which resulted in the compressive-to-tensile stress transformation.

In practical terms, it is thus expedient to perform the deposition process in the transition mode, which implies a significant exceedance of the deposition rate in the oxide mode. Afterwards, dead-load annealing can be conducted.

FUNDING

This work was financially supported by the Ministry of Science and Higher Education of the Russian Federation (Project no. 075-15-2021-1348, event no. 1.1.2).

CONFLICT OF INTEREST

The authors declare no conflict of interest.

REFERENCES

1. M. Mogensen, N. M. Sammes, and G. A. Tompset, Solid State Ionics **129**, 63 (2000). http://www.doi.org/10.1016/S0167-2738(99)00318-5
2. B. C. H. Steele, Solid State Ionics **129**, 95 (2000). http://www.doi.org/10.1016/S0167-2738(99)00319-7
3. J. L. M. Rupp, A. Infortuna, and L. J. Gauckler, J. Am. Ceram. Soc. **90**, 1792 (2007). http://www.doi.org/10.1111/j.1551-2916.2007.01531.x
4. H. C. Park and A. V. Virkar, J. Power Sources **186**, 133 (2009). http://www.doi.org/10.1016/j.jpowsour.2008.09.080
5. S. Cho, Y. Kim, J. Kim, A. Manthiram, and H. Wang, Electrochim. Acta **56**, 5472 (2011). http://www.doi.org/10.1016/j.electacta.2011.03.039
6. E. G. Kalinina and E. Y. Pikalova, Russ. Chem. Rev. **90**, 703 (2021). http://www.doi.org/10.1070/RCR4966
7. H. Yakabe, Y. Baba, T. Sakurai, and Y. Yoshitaka, J. Power Sources **135**, 9 (2004). http://www.doi.org/10.1016/j.jpowsour.2003.11.04
8. A. Atkinson, Solid State Ionics **95**, 249 (1997). http://www.doi.org/10.1016/s0167-2738(96)00588-7
9. C. S. Montross, H. Yokokawa, and M. Dokiya, Br. Ceram. Trans. **101**, 85 (2002). http://www.doi.org/10.1179/096797802225003956
10. B. Sun, R. A. Rudkin, and A. Atkinson, Fuel Cells **9**, 805 (2009). http://www.doi.org/10.1002/fuce.200800133
11. W. Fischer, J. Malzbender, G. Blass, and R. W. Steinbrech, J. Power Sources **150**, 73 (2005). http://www.doi.org/10.1016/j.jpowsour.2005.02.014
12. A. R. Shugurov and A. V. Panin, Tech. Phys. **65**, 1881 (2020). http://www.doi.org/10.1134/S1063784220120257
13. F. M. D'Heurle and J. M. Harper, Thin Solid Films **171**, 81 (1989). http://www.doi.org/10.1016/0040-6090(89)90035-7
14. O. Stenzel, S. Wilbrandt, N. Kaiser, M. Vinnichenko, F. Munnik, A. Kolitsch, A. Chuvilin, U. Kaiser, J. Ebert, and S. Jakobs, Thin Solid Films **517**, 6058 (2009). http://www.doi.org/10.1016/j.tsf.2009.05.009
15. J. Bae, I. Chang, S. Kang, S. Hong, S. W. Cha, and Y. B. Kim, J. Nanosci. Nanotechnol. **14**, 9294 (2014). http://www.doi.org/10.1166/jnn.2014.10121
16. W. Wu, Z. Liu, Z. Zhao, X. Zhang, D. Ou, B. Tu, D. Cui, and M. Cheng, Chin. J. Catal. **35**, 1376 (2014). http://www.doi.org/10.1016/s1872-2067(14)60137-6
17. J. Musil, P. Baroch, J. Vlček, K. H. Nam, and J. G. Han, Thin Solid Films **475**, 208 (2005). http://www.doi.org/10.1016/j.tsf.2004.07.041
18. S. Berg, T. Nyberg, and T. Kubart, Modelling of reactive sputtering processes, in *Reactive Sputter Deposition*, Ed. D. Depla and S. Mahieu (Springer, New York, 2008).
19. A. Solovyev, I. Ionov, A. Lauk, S. Linnik, A. Shipilova, and E. Smolyanskiy, J. Electrochem. Energy Convers. Storage **15**, 044501 (2018). http://www.doi.org/10.1115/1.4039705
20. G. C. A. M. Janssen, M. M. Abdalla, F. van Keulen, B. R. Pujada, and B. van Venrooy, Thin Solid Films **517**, 1858 (2009). http://www.doi.org/10.1016/j.tsf.2008.07.014
21. M. Pihlatie, A. Kaiser, and M. Mogensen, J. Eur. Ceram. Soc. **29**, 1657 (2009). http://www.doi.org/10.1016/j.jeurceramsoc.2008
22. S. Giraud and J. Canel, J. Eur. Ceram. Soc. **28**, 77 (2008). http://www.doi.org/10.1016/j.jeurceramsoc.2007.05.009
23. S. L. Fernandes, L. G. S. Albano, L. J. Affonco, J. H. D. Silva, E. Longo, and C. F. Graeff, Front. Chem. **7**, 50 (2019). http://www.doi.org/10.3389/fchem.2019.00050
24. D. J. Quinn, B. Wardle, and S. M. Spearing, J. Mater. Res. **23**, 609 (2008). http://www.doi.org/10.1557/jmr.2008.0077
25. A. Atkinson and A. Selcuk, Acta Mater. **47**, 867 (1999). http://www.doi.org/10.1016/s1359-6454(98)00412-1
26. L. Jia, Z. Lu, J. Miao, Z. Liu, G. Li, and W. Su, J. Alloys Compd. **414**, 152 (2006). http://www.doi.org/10.1016/j.jallcom.2005.03.119
27. A. A. Solovyev, S. V. Rabotkin, A. V. Shipilova, and I. V. Ionov, Int. J. Electrochem. Sci. **14**, 575 (2019). http://www.doi.org/10.20964/2019.01.03
28. W. Araki, Y. Imai, and T. Adachi, J. Eur. Ceram. Soc. **29**, 2275 (2009). http://www.doi.org/10.1016/j.jeurceramsoc.2009.01.014